Muon g-2: BMW calculation of the hadronic vacuum polarization contribution

Balint Toth, Szabolcs Borsanyi, Zoltan Fodor, Jana Guenther, Christian Hoelbling, Sandor Katz, Laurent Lellouch, Thomas Lippert, Kohtaroh Miura, Letizia Parato, et al.

PROCEEDINGS OF SCIENCE

Muon $g-2$: BMW calculation of the hadronic vacuum polarization contribution

B. C. Toth,[a,*] **Sz. Borsanyi,**[a] **Z. Fodor,**[a,b,c,d,e] **J. N. Guenther,**[a,f] **C. Hoelbling,**[a] **S. D. Katz,**[d] **L. Lellouch,**[f] **T. Lippert,**[a,b] **K. Miura,**[f,g,h] **L. Parato,**[f] **K. K. Szabo,**[a,b] **F. Stokes,**[a,b] **Cs. Torok**[b] **and L. Varnhorst**[a,f]

[a] *Department of Physics, University of Wuppertal, D-42119 Wuppertal, Germany*
[b] *Jülich Supercomputing Centre, Forschungszentrum Jülich, D-52428 Jülich, Germany*
[c] *Department of Physics, Pennsylvania State University, University Park, PA 16802, USA*
[d] *Institute for Theoretical Physics, Eötvös University, H-1117 Budapest, Hungary*
[e] *University of California, San Diego, 9500 Gilman Drive, La Jolla, CA 92093, USA*
[f] *Aix Marseille Univ, Université de Toulon, CNRS, CPT, IPhU, Marseille, France*
[g] *Helmholtz Institute Mainz, D-55099 Mainz, Germany*
[h] *Kobayashi-Maskawa Institute for the Origin of Particles and the Universe, Nagoya University, Nagoya 464-8602, Japan*

E-mail: btoth@uni-wuppertal.de

We compute the leading order hadronic vacuum polarization contribution to the anomalous magnetic moment of the muon. The calculations are performed using four flavors of stout smeared staggered quarks, with quark masses at their physical values. The continuum limit is taken using six different lattice spacings ranging from 0.132 fm down to 0.064 fm. All strong isospin breaking and electromagnetic effects are accounted for to leading order. A controlled infinite volume limit is taken thanks to dedicated simulations performed in box sizes up to 11 fm. Putting all these ingredients together, we find $[(g_\mu - 2)/2]_{\text{LO-HVP}} = 707.5[5.5] \times 10^{-10}$, which has a total uncertainty of 0.8%. Compared to determinations based on the $e^+e^- \to$ hadrons cross section, our result significantly reduces the tension between the standard model prediction for the muon $g-2$ and its experimental value.

The 38th International Symposium on Lattice Field Theory, LATTICE2021 26th-30th July, 2021 Zoom/Gather@Massachusetts Institute of Technology

*Speaker

1. Introduction

The muon is an ephemeral sibling of the electron. It is 207 times more massive, but has the same electric charge and spin. Similarly to the electron, it behaves like a tiny magnet, characterized by a magnetic moment. This quantity is proportional to the spin and charge of the muon, and inversely proportional to twice its mass. Dirac's relativistic quantum mechanics predicts that the constant of proportionality, g_μ, should be 2. However, in a relativistic quantum field theory such as the standard model, this prediction receives small corrections due to quantum, vacuum fluctuations. These corrections are called the anomalous magnetic moment and are quantified by $(g_\mu - 2)/2$. They were measured to an exquisite 0.54 ppm at the Brookhaven National Laboratory in the early 2000s [1], confirmed recently by Fermilab [2], and have been calculated with a comparable precision (see [3] for a recent review).

At this level of precision, all of the interactions of the standard model contribute. The leading contributions are electromagnetic and described by quantum electrodynamics (QED), but the one that dominates the theory error is induced by the strong interaction and requires solving the highly non-linear equations of quantum chromodynamics (QCD) at low energies. This contribution is determined by the leading-order, hadronic vacuum polarization (LO-HVP), which describes how the propagation of a virtual photon is modified by the presence of quark and gluon fluctuations in the vacuum. Here we compute this LO-HVP contribution to $(g_\mu - 2)/2$, denoted by $a_\mu^{\mathrm{LO-HVP}}$, using *ab initio* simulations in QCD and QED. In the present work, we include both QED and QCD, as well as four non-degenerate quark flavors (up, down, strange and charm), in a lattice formulation taking into account all dynamical effects. We also consider the tiny contributions of the bottom and top quarks.

We compute $a_\mu^{\mathrm{LO-HVP}}$ in the so-called time-momentum representation [4], which relies on the following, zero three-momentum, two-point function in Euclidean time t:

$$G(t) = \frac{1}{3e^2} \sum_{\mu=1,2,3} \int d^3x \langle J_\mu(\vec{x}, t) J_\mu(0) \rangle \,, \tag{1}$$

where J_μ is the quark electromagnetic current with $J_\mu/e = \frac{2}{3}\bar{u}\gamma_\mu u - \frac{1}{3}\bar{d}\gamma_\mu d - \frac{1}{3}\bar{s}\gamma_\mu s + \frac{2}{3}\bar{c}\gamma_\mu c$. u, d, s and c are the up, down, strange and charm quark fields and the angle brackets stand for the QCD+QED expectation value to order e^2. It is convenient to decompose $G(t)$ into light, strange, charm and disconnected components, which have very different statistical and systematic uncertainties. Integrating the one-photon-irreducible (1γI) part of the two-point function (1) yields the LO-HVP contribution to the magnetic moment of the muon [4–7]:

$$a_\mu^{\mathrm{LO-HVP}} = \alpha^2 \int_0^\infty dt \; K(t) \; G_{1\gamma\mathrm{I}}(t) \,, \tag{2}$$

with the weight function,

$$K(t) = \int_0^\infty \frac{dQ^2}{m_\mu^2} \, \omega\left(\frac{Q^2}{m_\mu^2}\right) \left[t^2 - \frac{4}{Q^2} \sin^2\left(\frac{Qt}{2}\right) \right] \,, \tag{3}$$

and where $\omega(r) = [r + 2 - \sqrt{r(r+4)}]^2 / \sqrt{r(r+4)}$, α is the fine structure constant in the Thomson limit and m_μ is the muon mass. Since we consider only the LO-HVP contribution, for brevity we

drop the superscript and multiply the result by 10^{10}, i.e. a_μ stands for $a_\mu^{\mathrm{LO-HVP}} \times 10^{10}$ throughout this work.

The subpercent precision, that we are aiming for, represents a huge challenge for lattice QCD. To reach that goal, we have to address the following critical issues: scale determination; noise reduction; QED and strong-isospin breaking; infinite-volume and continuum extrapolations. We briefly discuss these one by one. For a more detailed exposition we refer the reader to the Supplementary Information in [8].

2. Scale determination

The quantity a_μ depends on the muon mass. When computing (2) on the lattice, m_μ has to be converted into lattice units, am_μ, where a is the lattice spacing. A relative error of the lattice spacing propagates into about a twice as large a relative error on a_μ, so that a has to be determined with a few permil precision. We use the mass of the Ω^- baryon, $M_{\Omega^-} = 1672.45(29)$ MeV [9], to set the lattice spacing. Here we describe how we determine its QCD contribution; QED corrections are described below.

To extract the mass of the positive-parity, ground-state Ω baryon, a number of different operators are available in the staggered formalism. First, there are two operators from the pioneering work of Golterman and Smit [10]. To label these operators we use the convention of [11]:

$$\Omega_{\mathrm{VI}}(t) = \sum_{x_k \,\mathrm{even}} \epsilon_{abc} \left[S_1 \chi_a S_{12} \chi_b S_{13} \chi_c - S_2 \chi_a S_{21} \chi_b S_{23} \chi_c + S_3 \chi_a S_{31} \chi_b S_{32} \chi_c \right](x), \tag{4}$$

$$\Omega_{\mathrm{XI}}(t) = \sum_{x_k \,\mathrm{even}} \epsilon_{abc} [S_1 \chi_a S_2 \chi_b S_3 \chi_c](x). \tag{5}$$

Here, $\chi_a(x)$ is the strange-quark field with color index a. The operator S_μ performs a symmetric, gauge-covariant shift in direction μ, while $S_{\mu\nu} \equiv S_\mu S_\nu$. Both Ω_{VI} and Ω_{XI} couple to two different tastes of the Ω baryon, which become degenerate in the continuum limit. At finite lattice spacing however, there is a splitting between the two tastes. In principle they could be disentangled by carrying out an analysis involving the correlators of both Ω_{VI} and Ω_{XI} and also their cross terms. Later, Bailey successfully constructed an operator which only couples to a single taste [12]. To achieve this, two additional (valence) strange quarks are introduced: the strange-quark field gets an additional "flavor" index: $\chi_{a\alpha}$ with $\alpha = 1, 2, 3$. The operator is then given as

$$\begin{aligned} \Omega_{\mathrm{Ba}}(t) = &\left[2\delta_{\alpha 1}\delta_{\beta 2}\delta_{\gamma 3} - \delta_{\alpha 3}\delta_{\beta 1}\delta_{\gamma 2} - \delta_{\alpha 2}\delta_{\beta 3}\delta_{\gamma 1} + (\ldots \beta \leftrightarrow \gamma \ldots) \right] \cdot \\ &\cdot \sum_{x_k \,\mathrm{even}} \epsilon_{abc} \left[S_1 \chi_{a\alpha} S_{12} \chi_{b\beta} S_{13} \chi_{c\gamma} - S_2 \chi_{a\alpha} S_{21} \chi_{b\beta} S_{23} \chi_{c\gamma} + S_3 \chi_{a\alpha} S_{31} \chi_{b\beta} S_{32} \chi_{c\gamma} \right](x). \end{aligned} \tag{6}$$

The mass of this state becomes degenerate with the above two taste partners in the continuum limit. We investigated the difference between these three operators on an ensemble with large statistics. At $\beta = 3.7000$, corresponding to our coarsest lattice spacing, we computed the corresponding Ω propagators on about 3000 configurations in addition to those used for the current propagator measurements. The effective masses for the above three operators are shown in Figure 1. In the asymptotic regime we see deviations below 0.1%, which gives an estimate of the taste violation. We expect that these will get smaller as we go to finer lattice spacings. In this work we chose the Ω_{VI}

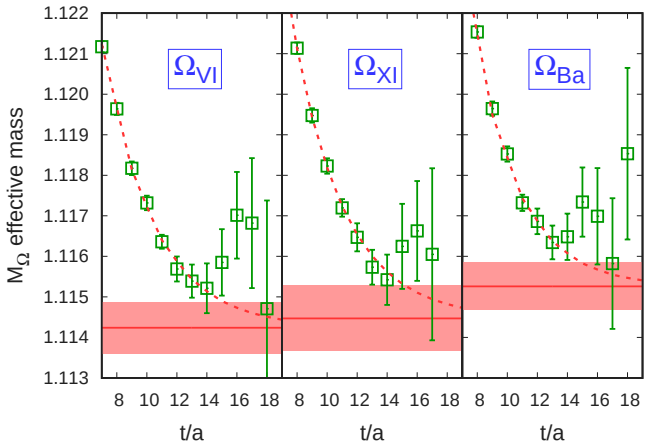

Figure 1: Effective mass of the ground state of the Ω baryon in lattice units on our coarsest ensemble with $\beta = 3.7000$. Results with three different staggered operators, Ω_{VI}, Ω_{XI} and Ω_{Ba} are shown. The horizontal lines and the shaded regions represent the fit values and the errors obtained with a four-state fit, Equation (7). The dashed lines are the effective masses computed from the fitted functions.

operator for our scale setting measurements. This is justified, since typical statistical and systematic errors on our ensembles are around 0.1%, and thus cover the taste-violation effects estimated here.

On the Ω propagators we perform a four-state fit using the fit function h, with two positive and two negative parity states:

$$h(t, A, M) = A_0 h_+(M_0, t) + A_1 h_-(M_1, t) + A_2 h_+(M_2, t) + A_3 h_-(M_3, t) \tag{7}$$

with $h_+(M,t) = e^{-Mt} + (-1)^{t-1} e^{-M(T-t)}$ and $h_-(M,t) = -h_+(M, T-t)$ describing the time dependence of the positive and negative parity states. Here M_0 and A_0 are the mass and amplitude of the ground state. In order to stabilize the fit, a prior term was introduced, containing priors on the masses except for the ground state. The prior for the negative parity ground state, $M_1 = 2012$ MeV, is motivated by the recent observation from the Belle collaboration [13]. The excited states, $M_2 = 2250$ MeV and $M_3 = 2400$ MeV, have not been discovered in experiments so far, so their priors follow from the quark model [14]. The existence of these undiscovered states is also motivated by lattice thermodynamics below the chiral transition [15, 16].

In addition to the above four-state fit to the Ω propagator we also used a mass extraction procedure proposed in [17], which is based on the Generalized Eigenvalue Problem (GEVP). The method has the advantage of not using priors.

For each time slice t we construct a 4×4 matrix $\mathcal{H}_{i,j}(t) = H_{t+(i-1)+(j-1)}$ $(i, j = 1, \ldots, 4)$, from the hadron propagator H_t. Then for a given t_a and t_b let $\lambda(t_a, t_b)$ be an eigenvalue and $v(t_a, t_b)$ an eigenvector solution to this 4×4 generalized eigenvalue problem:

$$\mathcal{H}(t_a) v(t_a, t_b) = \lambda(t_a, t_b) \mathcal{H}(t_b) v(t_a, t_b). \tag{8}$$

Here we select the smallest eigenvalue λ and use the corresponding eigenvector v to project out the ground state:

$$v^+(t_a, t_b) \mathcal{H}(t) v(t_a, t_b), \tag{9}$$

which then can be fitted to a simple $\exp(-Mt)$ type function.

The mass extracted using the GEVP gives a third M_Ω value for each ensemble, beside the results with the four-state fit procedure with two fit ranges. We will use the deviation between these three values as a systematic error in the Ω mass determination. More details on the scale determination can be found in Ref. [18] and in the Supplementary Information of [8].

3. Isospin-breaking effects

Our staggered path integral includes four flavors of quarks, $f = \{u, d, s, c\}$, gluon fields U and photon fields A and is given by:

$$Z = \int [dU] \exp(-S_g[U]) \int [dA] \exp(-S_\gamma[A]) \prod_f \det M^{1/4}[V_U \exp(ieq_f A), m_f]. \tag{10}$$

The photon integral measure $[dA]$ and action S_γ are defined in the $\mathrm{QED_L}$ scheme [19]. The one-hop staggered matrix in a background field W_μ can be written as

$$M[W, m] = D[W] + m = \sum_\mu D_\mu[W_\mu] + m, \tag{11}$$

where D_μ is the covariant differentiation in the μ direction involving W and its adjoint $W^\dagger$ together with the obligatory staggered phases. In the path integral the fermions are coupled to a gauge field that is a product of the exponentiated photon field and of the smeared gluon gauge field V_U. $q_f \in \{+\frac{2}{3}, -\frac{1}{3}, -\frac{1}{3}, +\frac{2}{3}\}$ stand for the quark electric charges in units of the positron charge e, m_f for the quark masses and $\alpha = e^2/(4\pi)$. We use the notation $\delta m \equiv m_d - m_u$ for the difference in the up and down quark masses and $m_l \equiv \frac{1}{2}(m_u + m_d)$ for their average. To simplify later formulas we also introduce the notations

$$M_f \equiv M[V_U e^{ieq_f A}, m_f] \qquad \text{and} \qquad \mathrm{dets}[U, A; \{m_f\}, \{q_f\}, e] \equiv \prod_f \det M_f^{1/4}, \tag{12}$$

where the latter is the product of all fermion determinants.

In this work isospin-breaking is implemented by taking derivatives with respect to the isospin-breaking parameters and by measuring the so obtained derivative operators on isospin-symmetric configurations [20]. We introduce a set of notations for isospin-symmetric observables and their isospin-breaking derivatives. Consider the observable $X(e, \delta m)$, which is a function of e and δm. Then we define

$$X_0 \equiv X(0,0), \qquad X'_m \equiv m_l \frac{\partial X}{\partial \delta m}(0,0), \qquad X'_1 \equiv \frac{\partial X}{\partial e}(0,0), \qquad X''_2 \equiv \frac{1}{2}\frac{\partial^2 X}{\partial e^2}(0,0). \tag{13}$$

We take into account only leading-order isospin-breaking in this work, so no higher derivatives are needed.

In the case of the fermion determinant, the isospin-symmetric value is denoted by dets_0. Since dets is symmetric under the exchange $u \leftrightarrow d$, the strong-isospin-breaking of dets is zero at leading

order: $\text{dets}'_m = 0$. The electromagnetic derivatives are

$$\begin{aligned}\frac{\text{dets}'_1}{\text{dets}_0} &= \sum_f \frac{q_f}{4}\text{Tr}\left(M_f^{-1}D[iAV_U]\right), \\ \frac{\text{dets}''_2}{\text{dets}_0} &= \frac{1}{2}\left[\left(\frac{\text{dets}'_1}{\text{dets}_0}\right)^2 - \sum_f \frac{q_f^2}{4}\text{Tr}\left(M_f^{-1}D[A^2V_U]\right) - \sum_f \frac{q_f^2}{4}\text{Tr}\left(M_f^{-1}D[iAV_U]M_f^{-1}D[iAV_U]\right)\right],\end{aligned} \tag{14}$$

where Tr is trace over color and spacetime indices and the argument of the D operator is a 3×3 complex matrix valued field, e.g. A^2V_U has components $A^2_{\mu,x}[V_U]_{\mu,x}$. The implementation of these derivatives is detailed in Refs. [8, 21].

We also make a distinction between the electric charge in the fermion determinant and in the operator that we measure. We call the former sea electric charge and denote it by e_s, the latter is the valence electric charge and is denoted by e_v. For an observable X that depends on both the valence and sea charges, $X(e_v, e_s)$, the second order electric charge derivatives are defined as follows:

$$X''_{20} \equiv \frac{1}{2}\frac{\partial^2 X}{\partial e_v^2}(0,0), \qquad X''_{11} \equiv \frac{\partial^2 X}{\partial e_v \partial e_s}(0,0), \qquad X''_{02} \equiv \frac{1}{2}\frac{\partial^2 X}{\partial e_s^2}(0,0). \tag{15}$$

For functions that depend on either e_v or e_s, but not on both, we use the single digit notations of Equation (13).

The expectation value of an operator O is calculated by inserting $O[U, A]$ into the integrand of the path integral of Equation (10) and normalizing the integral by Z. Here we consider operators whose photon field dependence arises entirely from the photon-quark interaction, i.e. $O = O[U, e_v A]$. The expectation value of this operator depends on δm, e_v and e_s, and the expansion in isospin breaking corrections can be written as:

$$\langle O\rangle = [\langle O\rangle]_0 + e_v^2\langle O\rangle''_{20} + e_v e_s\langle O\rangle''_{11} + e_s^2\langle O\rangle''_{02} + \tfrac{\delta m}{m_l}\langle O\rangle'_m. \tag{16}$$

Here, the individual terms can be expressed as expectation values obtained with the isospin-symmetric path integral, which we denote by $\langle\ldots\rangle_0$. The concrete expressions are:

$$\begin{aligned}\text{isospin-symmetric:} &\quad [\langle O\rangle]_0 = \langle O_0\rangle_0 \\ \text{qed valence-valence:} &\quad \langle O\rangle''_{20} = \langle O''_2\rangle_0 \\ \text{qed sea-valence:} &\quad \langle O\rangle''_{11} = \left\langle O'_1\frac{\text{dets}'_1}{\text{dets}_0}\right\rangle_0 \\ \text{qed sea-sea:} &\quad \langle O\rangle''_{02} = \left\langle O_0\frac{\text{dets}''_2}{\text{dets}_0}\right\rangle_0 - \langle O_0\rangle_0\left\langle\frac{\text{dets}''_2}{\text{dets}_0}\right\rangle_0 \\ \text{strong-isospin-breaking:} &\quad \langle O\rangle'_m = \langle O'_m\rangle_0\end{aligned} \tag{17}$$

In the derivation of these expressions we use $\left\langle\frac{\text{dets}'_1}{\text{dets}_0}\right\rangle_0 = 0$.

Note that Equation (16) is an expansion in bare parameters and not what we consider a decomposition into isospin-symmetric and isospin breaking parts. The latter involves derivatives with respect to renormalized observables and our prescription for that is given in Section 3.1. There is no need to introduce a renormalized electromagnetic coupling though: its running is an $O(e^4)$ effect, i.e. beyond the leading order isospin approximation that we consider here.

3.1 Isospin-breaking decomposition

For various purposes it is useful to decompose the observables into isospin-symmetric and isospin-breaking parts. This requires a matching of the isospin symmetric and full theories, in which we specify a set of observables that must be equal in both theories. Of course, different sets will lead to different decompositions, which is commonly referred to as scheme dependence. Only the sum of the components, i.e. the result in the full theory, is scheme independent.

A possible choice for the observables are the Wilson-flow–based w_0 scale and the masses of mesons built from an up/down/strange and an anti-up/down/strange quark, $M_{uu}/M_{dd}/M_{ss}$. These mesons are defined by taking into account only the quark-connected contributions in their two-point functions [22]. Their masses are practical substitutes for the quark masses. Also, they are neutral and have no magnetic moment, so they are a reasonable choice for an isospin decomposition. These masses cannot be measured in experiments, but have a well defined continuum limit and thus a physical value can be associated to them. In particular, we use the combinations $M^2_{\pi_\chi} \equiv \frac{1}{2}(M^2_{uu} + M^2_{dd})$ and $\Delta M^2 \equiv M^2_{dd} - M^2_{uu}$. For the determination of the physical values of w_0, M_{ss} and ΔM^2, see the Supplementary Information of [8].

For the decomposition we start with the QCD+QED theory and parameterize our observable $\langle O \rangle$ with the quantities defined above:

$$\langle O \rangle (M_{\pi_\chi} w_0, M_{ss} w_0, \tfrac{L}{w_0}, \Delta M w_0, e) \ . \tag{18}$$

Here, the continuum limit is assumed. We can isolate the electromagnetic part by switching off the electromagnetic coupling, while keeping the other parameters fixed. The strong-isospin-breaking part is given by the response to the ΔM parameter, and the isospin-symmetric part is just the remainder:

$$\langle O \rangle_{\text{qed}} \equiv e^2 \cdot \frac{\partial \langle O \rangle}{\partial e^2}\bigg|_{M_{\pi_\chi} w_0, M_{ss} w_0, \frac{L}{w_0}, \Delta M w_0, e=0} \tag{19}$$

$$\langle O \rangle_{\text{sib}} \equiv (\Delta M w_0)^2 \cdot \frac{\partial \langle O \rangle}{\partial (\Delta M w_0)^2}\bigg|_{M_{\pi_\chi} w_0, M_{ss} w_0, \frac{L}{w_0}, \Delta M w_0 = 0, e=0} \tag{20}$$

$$\langle O \rangle_{\text{iso}} \equiv \langle O \rangle (M_{\pi_\chi} w_0, M_{ss} w_0, \tfrac{L}{w_0}, 0, 0). \tag{21}$$

One can also define the decomposition at a finite lattice spacing, for which w_0 in lattice units can be additionally fixed. In doing so the isospin symmetric part $\langle O \rangle_{\text{iso}}$ has to be distinguished from the value of the observable at the bare isospin-symmetric point $[\langle O \rangle]_0$.

4. Noise reduction techniques

In this section we consider quantities at the isospin-symmetric point; noise reduction techniques for the isospin-breaking part are discussed in Refs. [8, 21]. For the strange and charm connected contributions, C_0^{strange} and C_0^{charm}, and for the disconnected contribution C_0^{disc} we use the same measurements that are presented in our previous work [23]. A new measurement procedure is implemented for the light connected component C_0^{light}. It is used to reanalyze the old configurations and make measurements on new ensembles. This plays a key role in reducing the final statistical error in a_μ.

4.1 Low Mode Averaging

The technique utilizes the lowest eigenmodes of the fermion matrix; for an early work with low eigenmodes, see [24]. The way in which we use these modes here is essentially the same as in [25], where it is called Low Mode Substitution. In the space orthogonal to these modes, the computational effort is reduced considerably by applying imprecise (aka. sloppy) matrix inversions. This is called the Truncated Solver Method [26] or All Mode Averaging [27]. Here we describe the technique for the connected part of the current propagator. The same technique was applied recently for magnetic moment computations in [28] also.

We consider the connected current propagator for timelike separation, and perform an averaging over the source positions, together with a zero spatial-momentum projection at the sink:

$$C(t,\bar{t}) \equiv \frac{1}{3L^3} \sum_{\vec{\bar{x}},\vec{x},\mu=1,2,3} C^{\text{conn}}_{\mu,x,\mu,\bar{x}}(m_l,0) = -\frac{1}{12L^3} \sum_{\mu=1,2,3} \text{ReTr}\left[\mathcal{D}_{\mu,t} M^{-1} \mathcal{D}_{\mu,\bar{t}} M^{-1}\right], \tag{22}$$

where $\mathcal{D}_{\mu,t} = \sum_{\vec{x}} D_\mu[iP_x U]$ is an operator that performs a symmetric, gauge-covariant shift on a vector v_x:

$$[\mathcal{D}_{\mu,t} v]_x = i\eta_{\mu,x} \left(U_{\mu,x} v_{x+\mu} + U^\dagger_{\mu,x-\mu} v_{x-\mu}\right) \cdot \delta_{x_4,t}\ , \tag{23}$$

where $\eta_{\mu,x}$ are the staggered phases. We use the simplifying notation $\mathcal{D} = \mathcal{D}_{\mu,t}$ and $\overline{\mathcal{D}} = \mathcal{D}_{\mu,\bar{t}}$ in the following. In Equation (22), we apply the real part to reduce noise, because the imaginary part vanishes anyway after averaging over gauge configurations.

Using the lowest eigenmodes of M we split the quark propagator into an eigenvector part and into its orthogonal complement, denoted by "e" and "r", respectively:

$$M^{-1} = M_e^{-1} + M_r^{-1}, \qquad M_e^{-1} = \sum_i \frac{1}{\lambda_i} v_i v_i^\dagger \qquad \text{and} \qquad M_r^{-1} = M^{-1}\left(1 - \sum_i v_i v_i^\dagger\right), \tag{24}$$

where v_i/λ_i is the i-th eigenvector/eigenvalue of the operator M. Correspondingly, C splits into eigen-eigen, rest-eigen and rest-rest contributions:

$$C = C_{ee} + C_{re} + C_{rr} = -\frac{1}{4L^3} \sum_{\substack{p=e,r \\ q=e,r}} \text{ReTr}\left[\mathcal{D} M_p^{-1} \overline{\mathcal{D}} M_q^{-1}\right], \tag{25}$$

where an average over μ is assumed but not shown explicitely. The benefit of this decomposition is that the trace in the **eigen-eigen part** can be calculated exactly, and is thus equivalent to calculating the propagator with all possible sources in position space. This is the main ingredient for the noise reduction. Though no extra inversions are needed in this part, it has to be optimized carefully, since there is a double sum over the eigenmodes, where each term is a scalar product $v_i^\dagger \mathcal{D} v_j$. In the **rest-eigen part** we have terms $v_i^\dagger \mathcal{D} M_r^{-1} \overline{\mathcal{D}} v_i$ and also terms where $\mathcal{D}$ and $\overline{\mathcal{D}}$ are exchanged. Therefore, this part is only a single sum over the eigenmodes, and each term involves one matrix inversion. Note that these inversions are preconditioned by the eigenvectors, so they need many fewer iterations than standard inversions. Additionally, we speed up the inversions by running them with a reduced precision, and for some randomly selected eigenvectors we correct for the small bias by adding the difference between a high precision solver and the reduced precision one [26, 27]. Finally, the **rest-rest part** is evaluated using random source vectors ξ: we calculate $\xi^\dagger \mathcal{D} M_r^{-1} \overline{\mathcal{D}} M_r^{-1} \xi$, which requires two inversions per random source. The reduced precision inverter technique is used here too. The improvement achieved by using these noise reduction techniques is shown in Figure 2.

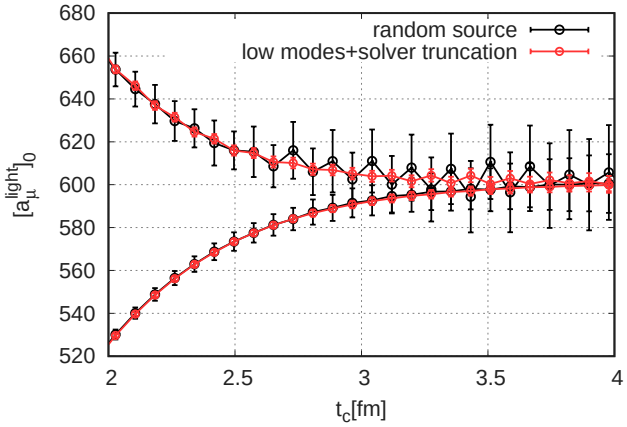

Figure 2: Comparison of a conventional random source based technique, as we applied it in our earlier work [23], and the low-mode improvement technique of this work on a $\beta = 3.9200$ `4stout` ensemble for the case of $[a_\mu^{\rm light}]_0$'s upper and lower bounds (see Section 4.2).

4.2 Upper and lower bounds on $\langle JJ \rangle$

In the case of the light and disconnected contributions to the current propagator, the signal deteriorates quickly as distance is increased. To calculate the HVP, a sum over time of the propagator has to be performed. As was suggested in [29, 30], we introduce a cut in time t_c, beyond which the propagator is replaced by upper and lower bounds, thereby reducing the statistical noise. Our estimate is given by the average of the bounds at a t_c where the two bounds meet. The bounds are derived from the fact that the current propagator is a sum of exponentials with positive coefficients.

For the **light connected propagator** at the isospin-symmetric point the bounds express the positivity (lower bound) and that the propagator should decay faster than the exponential of two pions (upper bound). They are given as

$$0 \le G^{\rm light}(t) \le G^{\rm light}(t_c)\frac{\varphi(t)}{\varphi(t_c)}, \tag{26}$$

where $\varphi(t) = \exp(-E_{2\pi}t)$. For $E_{2\pi}$ we use the energy of two non-interacting pions with the smallest non-zero lattice momentum $2\pi/L$. The larger the t_c the better the upper bound, but it comes with more statistical noise.

The exponential decay above assumes an infinite time extent, $T = \infty$. We incorporate the effects of a finite-T using next-to-leading-order chiral perturbation theory. There the exponential decay with the two-pion energy gets replaced by the following cosh-type form:

$$\exp(-E_{2\pi}t) \longrightarrow \frac{\cosh[E_{2\pi}(t - T/2)] + 1}{\cosh(E_{2\pi}T/2) - 1}\,. \tag{27}$$

In the case of the isospin-symmetric **disconnected propagator** the bounds are

$$0 \le -G^{\rm disc}(t) \le \tfrac{1}{10}G^{\rm light}(t_c)\frac{\varphi(t)}{\varphi(t_c)} + G^{\rm strange}(t) + G^{\rm charm}(t). \tag{28}$$

Since the strange and charm terms fall off much faster than the light and disconnected one, their contribution does not change the value of t_c obtained.

5. Finite-size effects

We compute finite-size effects on a_μ in a systematic way, which includes dedicated lattice simulations, chiral perturbation theory and phenomenological models. The concrete goal is to provide a single number that is to be added to the continuum-extrapolated lattice result obtained in a reference box, which is defined by a spatial extent of $L_{\text{ref}} = 6.272$ fm and a temporal extent of $T_{\text{ref}} = \frac{3}{2}L_{\text{ref}}$. For a more extensive description see Ref. [8].

We perform dedicated lattice simulations with two different lattice geometries: one is a 56×84 lattice with the reference box size and the other is a large 96×96 lattice with box size $L = L_{\text{big}} = 10.752$ fm and $T = T_{\text{big}} = L_{\text{big}}$. Since taste violations distort the finite-size effects, we designed a new action with highly-suppressed taste breaking, which we call `4HEX` (see [8]). Our strategy is then to compute the finite-size correction as the following sum:

$$\begin{aligned} a_\mu(\infty,\infty) - a_\mu(L_{\text{ref}},T_{\text{ref}}) = \\ = [a_\mu(L_{\text{big}},T_{\text{big}}) - a_\mu(L_{\text{ref}},T_{\text{ref}})]_{\texttt{4HEX}} + [a_\mu(\infty,\infty) - a_\mu(L_{\text{big}},T_{\text{big}})]_{\text{XPT}}. \end{aligned} \tag{29}$$

The first difference on the right hand side is taken from the dedicated `4HEX` simulations. The second difference is expected to be much smaller than the first and is taken from a non-lattice approach: two-loop chiral perturbation theory.

We consider four non-lattice approaches to compute both differences on the right hand side of Equation (29). In the case of the first difference, the results obtained are compared to our `4HEX` simulations. The first approach is chiral perturbation theory (XPT) to next-to-leading and next-to-next-to-leading orders (NLO and NNLO), the second is the Meyer-Lellouch-Luscher-Gounaris-Sakurai model (MLLGS), the third approach is that of Hansen and Patella (HP) [31] and the fourth is the rho-pion-gamma model of [32], which we abbreviate as RHO here.

We compute the first difference in Equation (29) using dedicated simulations with the `4HEX` action. We use the harmonic-mean-square (HMS) to set the physical point:

$$M^{-2}_{\pi,\text{HMS}} \equiv \frac{1}{16}\sum_\alpha M^{-2}_{\pi,\alpha}\,,$$

defined as an average over the masses of the 16 pion tastes, $M_{\pi,\alpha}$. We set $M_{\pi,\text{HMS}}$ to the physical value of the pion mass, which requires lowering the Goldstone-pion mass to 110 MeV. This way of fixing the physical point results in much smaller lattice artefacts than the usual setting with the Goldstone-pion, at least for an observable like the finite-size effect. To generate the `4HEX` data set, we performed simulations with two different Goldstone pion masses: $M_\pi = 104$ MeV and 121 MeV. To set the physical point as described above, we perform an interpolation from these two pion masses to $M_\pi = 110$ MeV.

To compute a_μ^{light} from the current propagator in our `4HEX` simulations we use the upper and lower bound technique described in Section 4.2. Results for the $M_\pi = 121$ MeV simulation point are plotted in Figure 3. The bounds meet at around 4.2 fm and 4.7 fm on the small and large volumes, respectively. At these distances we take the average of the two bounds as an estimate for a_μ^{light}.

We only have one lattice spacing with the `4HEX` action, so the finite-size effects cannot be extrapolated to the continuum limit. We estimate the cutoff effect of the result by comparing a_μ^{light}

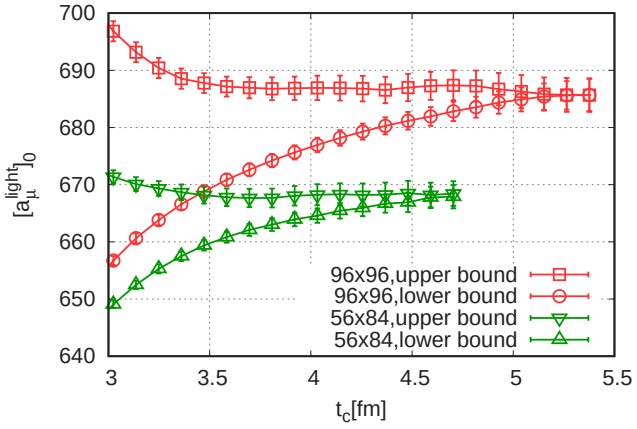

Figure 3: Upper and lower bounds on the light isospin-symmetric component of a_μ. The results shown here are obtained with the `4HEX` action on two different volumes at $a = 0.112$ fm lattice spacing and $M_\pi = 121$ MeV Goldstone-pion mass. We also have another simulation with $M_\pi = 104$ MeV mass. From these two we interpolate to $M_\pi = 110$ MeV.

with the `4HEX` action at this single lattice spacing to the continuum extrapolated `4stout` lattice result, both in the L_{ref} volume. The `4HEX` result is about 7% larger than the continuum value. Therefore we reduce the measured finite-size effect by 7%, and assign a 7% uncertainty to this correction step. For the difference we get

$$a_\mu(L_{\text{big}}, T_{\text{big}}) - a_\mu(L_{\text{ref}}, T_{\text{ref}}) = 18.1(2.0)_{\text{stat}}(1.4)_{\text{cont}} \,. \tag{30}$$

The result includes a $\left(\frac{9}{10}\right)$ charge factor, and the first error is statistical and the second is an estimate of the cutoff effect.

The finite-size effects computed in various non-lattice approaches are collected in Table 1. Except for the NLO result, the different models give finite-size effects of similar size, which agree well with the lattice determination of Equation (30). We also see that, according to the models, the finite-T effect is much smaller than the finite-L effect.

The good agreement for the finite-size effect in the reference box, between the models and the lattice, gives us confidence that the models can be used to reliably compute the very small, residual, finite-size effect of the large box. The corresponding model estimates can be found in Table 1. For an infinite-time extent the NNLO XPT, the HP and RHO approaches agree nicely. As a final value for the large-box, finite-size effect we take the NNLO XPT result including finite-T effects:

$$a_\mu(\infty, \infty) - a_\mu(L_{\text{big}}, T_{\text{big}}) = 0.6(0.3)_{\text{big}} \,,$$

where the uncertainty is an estimate of higher-order effects, given here by the difference of the NNLO and NLO values.

For our final result for the finite-size effect in the reference box, we also include the contribution of isoscalar channel and isospin-breaking effects giving:

$$a_\mu(\infty, \infty) - a_\mu(L_{\text{ref}}, T_{\text{ref}}) = 18.7(2.0)_{\text{stat}}(1.4)_{\text{cont}}(0.3)_{\text{big}}(0.6)_{I=0}(0.1)_{\text{qed}}[2.5] \,.$$

	NLO XPT	NNLO XPT	MLLGS	HP	RHO
$a_\mu(L_{\rm big}, T_{\rm big}) - a_\mu(L_{\rm ref}, T_{\rm ref})$	11.6	15.7	17.8	–	–
$a_\mu(L_{\rm big}, \infty) - a_\mu(L_{\rm ref}, \infty)$	11.2	15.3	17.4	16.3	14.8
$a_\mu(\infty, \infty) - a_\mu(L_{\rm big}, T_{\rm big})$	0.3	0.6	–	–	–
$a_\mu(\infty, \infty) - a_\mu(L_{\rm big}, \infty)$	1.2	1.4	–	1.4	1.4

Table 1: Finite-size effect in the reference box of the isospin-symmetric component of a_μ. The figures are obtained in various model approaches.

The first error is the statistical uncertainty of our `4HEX` computation, the second is an estimate of the `4HEX` cutoff effects, the third is the uncertainty of the residual finite-size effect of the "big" lattice, the fourth is a XPT estimate of the $I = 0$ finite size effect and the fifth is an estimate of the isospin-breaking effects. The last, total error in the square-brackets is the sum of the first five, added in quadrature.

6. Taste improvement

As is well known, some of the most important cutoff effects of staggered fermions are taste violations. At long distances, these violations distort the pion spectrum. Since a_μ is predominantly a long-distance observable, dominated by a two-pion contribution, including the ρ resonance, we expect these effects to be largest in the light-quark terms.

We investigate various physically motivated models for reducing long-distance taste violations in our lattice results. We consider three techniques: next-to-next-to-leading order chiral perturbation theory (NNLO XPT), a Meyer-Lellouch-Lüscher-Gounaris-Sakurai model (MLLGS) and the rho-pion-gamma model (RHO). A detailed exposition of these models can be found in the Supplementary Material of Ref. [8]. We investigate and discuss the suitability of their staggered versions for reducing the taste violations present in our lattice data. We call the resulting corrections taste improvements, because they improve the continuum extrapolation of our lattice data without, in principle, modifying the continuum-limit value. Indeed, these corrections vanish in that limit, as taste-breaking effects should. These improvements are applied on light-quark observables at the isospin-symmetric point, whose taste violations have the largest impact on our final uncertainties.

The models NNLO XPT, MLLGS and RHO describe the long-distance physics associated with finite-volume effects, as measured in our simulations. One can also define corresponding models describing the taste violations, they are denoted NNLO SXPT, SMLLGS and SRHO. We find that they describe the physics associated with taste violations, at least at larger distances. This is illustrated in Figure 4, where cutoff effects in the integrand of $a_\mu^{\rm light}$ are plotted as a function of Euclidean time. More specifically, we define the physical observable, obtained by convoluting the integrand of $a_\mu^{\rm light}$ with a smooth window function

$$W(t; t_1, t_2) \equiv \Theta(t; t_1, \Delta) - \Theta(t; t_2, \Delta) \quad \text{with} \quad \Theta(t; t', \Delta) \equiv \tfrac{1}{2} + \tfrac{1}{2}\tanh[(t - t')/\Delta] \qquad (31)$$

of a width of $t_2 - t_1 = 0.5$ fm and starting at a time of t_1. Then we consider the difference in the value of this observable, obtained on a fine and a coarse lattice at a sequence of t_1 separated by

0.1 fm. These are compared to the NLO SXPT, NNLO SXPT, SRHO and SMLLGS predictions for this quantity, evaluated at the exact parameters of the ensembles.

The SMLLGS, the SRHO and the NNLO SXPT taste improvements describe the numerical data very nicely for $t_1 \gtrsim 2.0\,\text{fm}$, fairly well for $t_1 \gtrsim 1.0\,\text{fm}$ and all the way down to $t_1 \simeq 0.4\,\text{fm}$ in the case of SRHO. All three slightly overestimate the observed cutoff effects, the rho-meson based approach performing best, whereas NNLO displays a large deviation from the lattice results in the $t_1 \leq 0.8\,\text{fm}$ region. The lattice results have a maximum at $t_1 = 1.4\,\text{fm}$, as does the SRHO improvement, reinforcing our confidence that this model captures the relevant physics.

These findings lead us to apply the following taste corrections to our simulations results for $a_\mu^{\text{light}}(L,T,a)$, obtained on an $L^3 \times T$ lattice with lattice spacing a, before performing continuum extrapolations:

$$a_\mu^{\text{light}}(L,T,a) \to a_\mu^{\text{light}}(L,T,a) + \tfrac{10}{9}\left[a^{\text{RHO}}_{\mu,t\geq t_{\text{sep}}}(L_{\text{ref}},T_{\text{ref}}) - a^{\text{SRHO}}_{\mu,t\geq t_{\text{sep}}}(L,T,a)\right],$$

with $t_{\text{sep}} = 0.4, 0.7, 1.0, 1.3\,\text{fm}$, and where the factor $(10/9)$ is related to the quark charges. Note that by using L_{ref} and T_{ref} in the above Equation, we are applying a very small volume correction to interpolate all of our simulation results to the same reference, four-volume so that they can be extrapolated to the continuum limit together.

The taste-improved data is then extrapolated to the continuum using our standard fit procedure, in the course of which isospin-breaking effects are also included. For estimating the systematic error we use a histogram technique [8].

The procedure described above does not yet take into account the systematic uncertainty associated with our choice of SRHO for taste improvement for $t > 1.3\,\text{fm}$. Since applying no taste improvement in that region is not an option, because of the nonlinearities introduced by two-pion, taste violations, we turn to NNLO SXPT, only as a means to estimate the uncertainty associated with this choice. Thus, we define this systematic uncertainty as ERR = (SRHO − NNLO SXPT) for $t > 1.3\,\text{fm}$. Then, we perform the same histogram analysis but with SRHO, SRHO-ERR and SRHO+ERR improvements. From this histogram we extract the contribution which comes from the variation in the improvement model from SRHO-ERR to SRHO+ERR. We assign this full spread to the systematic uncertainty associated with the taste-improvement procedure. We add this error in quadrature to the error given by the histogram technique discussed in the previous paragraph.

7. Intermediate window

The work [33] defined a particularly useful observable $a_{\mu,\text{win}}$, in which the current propagator is restricted to a time window $[t_1, t_2]$, using the smooth weight function $W(t;t_1,t_2)$ defined in Equation (31). The advantage of $a_{\mu,\text{win}}$ over a_μ is that, by choosing an appropriate window, the calculation can be made much less challenging on the lattice than for the full a_μ. Here we will be interested in the window between $t_1 = 0.4$ fm and $t_2 = 1.0$ fm, i.e. in an intermediate time range. By this choice we eliminate both the short-distance region, where large cutoff effects are present, and the long-distance region, where the statistical uncertainties and finite-size effects are large. Moreover, in the case of staggered fermions, it has reduced taste-breaking artefacts. This is shown in Figure 5, where the light, connected component of $a_{\mu,\text{win}}$ is plotted as a function of

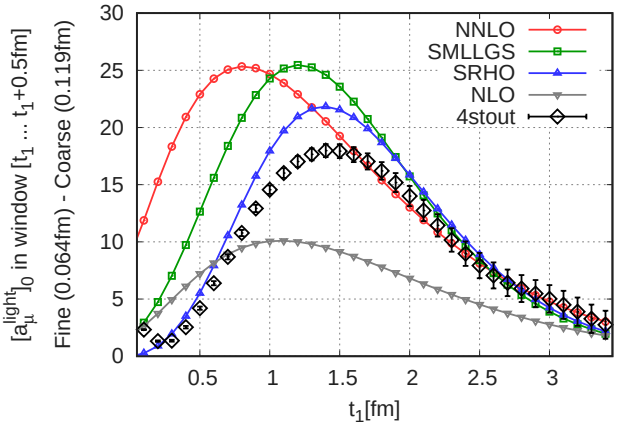

Figure 4: Isospin-symmetric component of a_μ^{light} computed with a sliding window. The window starts at t_1 and ends 0.5 fm later. The plot shows the difference between a fine and a coarse lattice, whose sizes are $L = 6.14\,\text{fm}$ and $L = 6.67\,\text{fm}$. The black squares with errors are obtained from the simulation. The colored curves are the predictions of NLO and NNLO SXPT, the SRHO and the SMLLGS models. They are computed at the parameters (pion mass, taste violation, volume) of the simulations.

a^2. Because the determination of this quantity does not require overcoming many of the challenges described above, other lattice groups have obtained it with errors comparable to ours [28, 33]. This allows for a sharper benchmarking of our calculation of this challenging, light-quark contribution that dominates a_μ. Our $a_{\mu,\text{win}}^{\text{light}}$ differs by 0.2σ and 2.2σ from the lattice results of [28] and [33], respectively. Moreover, $a_{\mu,\text{win}}$ can be computed in the R-ratio approach [8]. However, here we find a 3.7σ tension with our lattice result.

8. Conclusions

Combining all of these ingredients we obtain, as a final result, $a_\mu = 707.5(2.3)(5.0)[5.5]$. The first, statistical error comes mostly from the noisy, large-distance region of the current-current correlator. The second, systematic error is dominated by the continuum extrapolation and the finite-size effect computation. The third, total error is obtained by adding the first two in quadrature. In total we reach a relative accuracy of 0.8%.

Figure 6 compares our result with previous lattice computations and also with results from the R-ratio method, which have recently been reviewed in [3]. As one can see, there is a tension between our result and those obtained by the R-ratio method. For the total, LO-HVP contribution to a_μ, our result is 2.0σ, 2.5σ, 2.4σ and 2.2σ larger than the R-ratio results of $a_\mu = 694.0(4.0)$ [39], $a_\mu = 692.78(2.42)$ [34], $a_\mu = 692.3(3.3)$ [40, 41] and the combined result $a_\mu = 693.1(4.0)$ of [3], respectively. It is worth noting that the R-ratio determinations are based on the same experimental data sets and are therefore strongly correlated, though these data sets were obtained in several different and independent experiments that we have no reason to believe are collectively biased. Clearly, these comparisons need further investigation.

To conclude, when combined with the other standard model contributions (see eg. [3]), our result for the leading-order hadronic contribution to the anomalous magnetic moment of the muon,

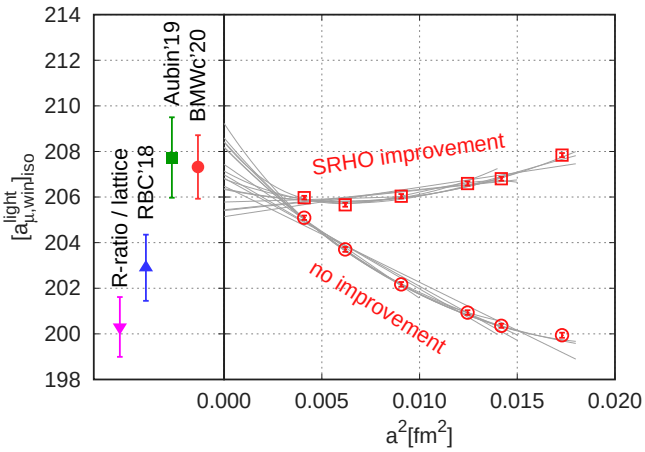

Figure 5: Continuum extrapolation of the isospin-symmetric, light, connected component of the window observable $a_{\mu,\mathrm{win}}$, denoted by $[a^{\mathrm{light}}_{\mu,\mathrm{win}}]_{\mathrm{iso}}$. The data points are extrapolated to the infinite-volume limit. Two different ways to perform the continuum extrapolations are shown: one without improvement, and another with corrections from a model involving the ρ-meson (SRHO). In both cases the lines show linear, quadratic and cubic fits in a^2 with varying number of lattice spacings in the fit. The continuum extrapolated result is shown with the results from other lattice groups, RBC'18 [33] and Aubin'19 [28]. Also plotted is our R-ratio-based determination, obtained using the experimental data compiled by the authors of [34] and our lattice results for the non light connected contributions. This plot is convenient for comparing different lattice results with each other. Regarding the total $a_{\mu,\mathrm{win}}$, for which we also have to include the contributions of other-than-light flavors and isospin-breaking effects, we obtain 236.7[1.4] on the lattice and 229.7[1.3] from the R-ratio, the latter is 3.7σ or 3.1% smaller than the lattice result.

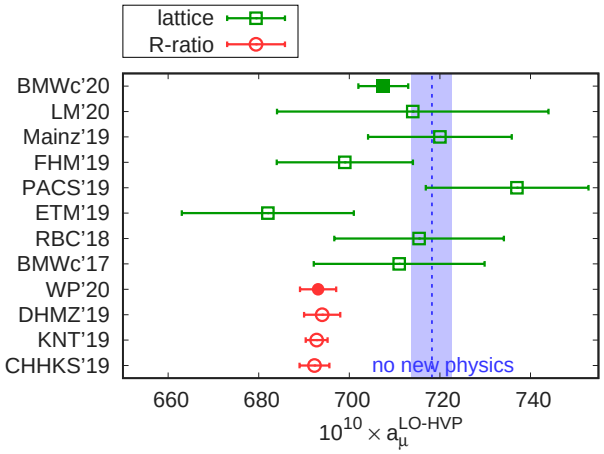

Figure 6: Comparison of recent results for the leading-order, hadronic vacuum polarization contribution to the anomalous magnetic moment of the muon. See [3] for a recent review. Green squares are lattice results: this work's result, denoted by BMWc'20 and represented by a filled symbol at the top of the figure, is followed by LM'20 [35], Mainz'19 [36], FHM'19 [37], ETM'19 [38], RBC'18 [33] and our earlier work BMWc'17 [23]. Red circles were obtained using the R-ratio method: the combined result WP'20 [3] is followed by DHMZ'19 [39], KNT'19 [34] and CHHKS'19 [40, 41]; these results use the same experimental data as input. The blue shaded region is the value that $a_\mu^{\mathrm{LO-HVP}}$ would have to have to explain the experimental measurement of $(g_\mu - 2)$, assuming no new physics.

weakens the longstanding discrepancy between experiment and theory. However, as discussed above and can be seen in Figure 6, our lattice result shows some tension with the R-ratio determinations. Obviously, our findings should be confirmed –or refuted– by other collaborations using other discretizations of QCD.

References

[1] **Muon g-2** Collaboration, G. W. Bennett *et. al.*, *Final Report of the Muon E821 Anomalous Magnetic Moment Measurement at BNL*, Phys. Rev. **D73** (2006) 072003 [hep-ex/0602035].

[2] **Muon g-2** Collaboration, B. Abi *et. al.*, *Measurement of the Positive Muon Anomalous Magnetic Moment to 0.46 ppm*, Phys. Rev. Lett. **126** (2021), no. 14 141801 [2104.03281].

[3] T. Aoyama *et. al.*, *The anomalous magnetic moment of the muon in the Standard Model*, Phys. Rept. **887** (2020) 1–166 [2006.04822].

[4] D. Bernecker and H. B. Meyer, *Vector Correlators in Lattice QCD: Methods and applications*, Eur. Phys. J. **A47** (2011) 148 [1107.4388].

[5] B. E. Lautrup, A. Peterman and E. de Rafael, *Recent developments in the comparison between theory and experiments in quantum electrodynamics*, Phys. Rept. **3** (1972) 193–259.

[6] E. de Rafael, *Hadronic contributions to the muon g-2 and low-energy QCD*, Phys. Lett. **B322** (1994) 239–246 [hep-ph/9311316].

[7] T. Blum, *Lattice calculation of the lowest order hadronic contribution to the muon anomalous magnetic moment*, Phys. Rev. Lett. **91** (2003) 052001 [hep-lat/0212018].

[8] S. Borsanyi *et. al.*, *Leading hadronic contribution to the muon magnetic moment from lattice QCD*, Nature **593** (2021), no. 7857 51–55 [2002.12347].

[9] **Particle Data Group** Collaboration, M. Tanabashi *et. al.*, *Review of Particle Physics*, Phys. Rev. **D98** (2018), no. 3 030001.

[10] M. F. L. Golterman and J. Smit, *Lattice Baryons With Staggered Fermions*, Nucl. Phys. **B255** (1985) 328–340.

[11] N. Ishizuka, M. Fukugita, H. Mino, M. Okawa and A. Ukawa, *Operator dependence of hadron masses for Kogut-Susskind quarks on the lattice*, Nucl. Phys. **B411** (1994) 875–902.

[12] J. A. Bailey, *Staggered baryon operators with flavor SU(3) quantum numbers*, Phys. Rev. **D75** (2007) 114505 [hep-lat/0611023].

[13] **Belle** Collaboration, J. Yelton *et. al.*, *Observation of an Excited Ω^- Baryon*, Phys. Rev. Lett. **121** (2018), no. 5 052003 [1805.09384].

[14] S. Capstick and N. Isgur, *Baryons in a Relativized Quark Model with Chromodynamics*, Phys. Rev. **D34** (1986) 2809. [AIP Conf. Proc.132,267(1985)].

[15] A. Bazavov *et. al.*, *Additional Strange Hadrons from QCD Thermodynamics and Strangeness Freezeout in Heavy Ion Collisions*, Phys. Rev. Lett. **113** (2014), no. 7 072001 [1404.6511].

[16] P. Alba *et. al.*, *Constraining the hadronic spectrum through QCD thermodynamics on the lattice*, Phys. Rev. **D96** (2017), no. 3 034517 [1702.01113].

[17] C. Aubin and K. Orginos, *A new approach for Delta form factors*, AIP Conf. Proc. **1374** (2011), no. 1 621–624 [1010.0202].

[18] L. Varnhorst *et. al.*, *High precision scale setting on the lattice*, PoS **LATTICE2021** (2022) 371.

[19] M. Hayakawa and S. Uno, *QED in finite volume and finite size scaling effect on electromagnetic properties of hadrons*, Prog. Theor. Phys. **120** (2008) 413–441 [0804.2044].

[20] **RM123** Collaboration, G. M. de Divitiis, R. Frezzotti, V. Lubicz, G. Martinelli, R. Petronzio, G. C. Rossi, F. Sanfilippo, S. Simula and N. Tantalo, *Leading isospin breaking effects on the lattice*, Phys. Rev. **D87** (2013), no. 11 114505 [1303.4896].

[21] L. Parato *et. al.*, *QED and strong isospin corrections in the hardonic vacuum polarization contribution to the anomalous magnetic moment of the muon*, PoS **LATTICE2021** (2022) 358.

[22] **Budapest-Marseille-Wuppertal** Collaboration, S. Borsanyi *et. al.*, *Isospin splittings in the light baryon octet from lattice QCD and QED*, Phys. Rev. Lett. **111** (2013), no. 25 252001 [1306.2287].

[23] **Budapest-Marseille-Wuppertal** Collaboration, S. Borsanyi *et. al.*, *Hadronic vacuum polarization contribution to the anomalous magnetic moments of leptons from first principles*, Phys. Rev. Lett. **121** (2018), no. 2 022002 [1711.04980].

[24] H. Neff, N. Eicker, T. Lippert, J. W. Negele and K. Schilling, *On the low fermionic eigenmode dominance in QCD on the lattice*, Phys. Rev. **D64** (2001) 114509 [hep-lat/0106016].

[25] **xQCD** Collaboration, A. Li *et. al.*, *Overlap Valence on 2+1 Flavor Domain Wall Fermion Configurations with Deflation and Low-mode Substitution*, Phys. Rev. **D82** (2010) 114501 [1005.5424].

[26] G. S. Bali, S. Collins and A. Schafer, *Effective noise reduction techniques for disconnected loops in Lattice QCD*, Comput. Phys. Commun. **181** (2010) 1570–1583 [0910.3970].

[27] T. Blum, T. Izubuchi and E. Shintani, *New class of variance-reduction techniques using lattice symmetries*, Phys. Rev. **D88** (2013), no. 9 094503 [1208.4349].

[28] C. Aubin, T. Blum, C. Tu, M. Golterman, C. Jung and S. Peris, *Light quark vacuum polarization at the physical point and contribution to the muon g − 2*, Phys. Rev. D **101** (2020), no. 1 014503 [1905.09307].

[29] C. Lehner RBRC Workshop on Lattice Gauge Theories (2016).

[30] S. Borsanyi, Z. Fodor, T. Kawanai, S. Krieg, L. Lellouch, R. Malak, K. Miura, K. K. Szabo, C. Torrero and B. C. Toth, *Slope and curvature of the hadronic vacuum polarization at vanishing virtuality from lattice QCD*, Phys. Rev. **D96** (2017), no. 7 074507 [1612.02364].

[31] M. T. Hansen and A. Patella, *Finite-volume effects in* $(g-2)_\mu^{HVP,LO}$, Phys. Rev. Lett. **123** (2019) 172001 [1904.10010].

[32] B. Chakraborty, C. T. H. Davies, P. G. de Oliviera, J. Koponen, G. P. Lepage and R. S. Van de Water, *The hadronic vacuum polarization contribution to a_μ from full lattice QCD*, Phys. Rev. **D96** (2017), no. 3 034516 [1601.03071].

[33] **RBC, UKQCD** Collaboration, T. Blum, P. A. Boyle, V. Gulpers, T. Izubuchi, L. Jin, C. Jung, A. Juttner, C. Lehner, A. Portelli and J. T. Tsang, *Calculation of the hadronic vacuum polarization contribution to the muon anomalous magnetic moment*, Phys. Rev. Lett. **121** (2018), no. 2 022003 [1801.07224].

[34] A. Keshavarzi, D. Nomura and T. Teubner, *$g-2$ of charged leptons, $\alpha(M_Z^2)$, and the hyperfine splitting of muonium*, Phys. Rev. **D101** (2020), no. 1 014029 [1911.00367].

[35] C. Lehner and A. S. Meyer, *Consistency of hadronic vacuum polarization between lattice QCD and the R-ratio*, Phys. Rev. D **101** (2020) 074515 [2003.04177].

[36] A. Gerardin, M. Ce, G. von Hippel, B. Horz, H. B. Meyer, D. Mohler, K. Ottnad, J. Wilhelm and H. Wittig, *The leading hadronic contribution to $(g-2)_\mu$ from lattice QCD with $N_f = 2+1$ flavours of O(a) improved Wilson quarks*, Phys. Rev. **D100** (2019), no. 1 014510 [1904.03120].

[37] **Fermilab Lattice, LATTICE-HPQCD, MILC** Collaboration, C. T. H. Davies *et. al.*, *Hadronic-Vacuum-Polarization Contribution to the Muon's Anomalous Magnetic Moment from Four-Flavor Lattice QCD*, Phys. Rev. **D101** (2020) 034512 [1902.04223].

[38] D. Giusti, V. Lubicz, G. Martinelli, F. Sanfilippo and S. Simula, *Electromagnetic and strong isospin-breaking corrections to the muon $g-2$ from Lattice QCD+QED*, Phys. Rev. **D99** (2019), no. 11 114502 [1901.10462].

[39] M. Davier, A. Hoecker, B. Malaescu and Z. Zhang, *A new evaluation of the hadronic vacuum polarisation contributions to the muon anomalous magnetic moment and to $\alpha(m_Z^2)$*, Eur. Phys. J. C **80** (2020), no. 3 241 [1908.00921].

[40] G. Colangelo, M. Hoferichter and P. Stoffer, *Two-pion contribution to hadronic vacuum polarization*, JHEP **02** (2019) 006 [1810.00007].

[41] M. Hoferichter, B.-L. Hoid and B. Kubis, *Three-pion contribution to hadronic vacuum polarization*, JHEP **08** (2019) 137 [1907.01556].